Electronic Supplementary Material (ESI) for Chemical Science.

Accelerated Active Phase Transformation of NiO Powered by Pt Single Atom for Enhanced Oxygen Evolution Reaction

Chao Lin, [a] Yonghui Zhao,[a] Haojie Zhang,[a] Songhai Xie,[b] Ye-Fei Li,*[b] Xiaopeng Li,*[a] Zheng Jiang,*[c] and Zhi-Pan Liu [b]

Experimental

Reagents. Chemical regents of ultrapure grade used as received without purification. The silica template was purchased from Grace Corporation (Davisil®). Electrolyte was rigorously treated to remove Fe impurities.

Synthesis of porous NiO, Pt/NiO, and PtO_2. In a typical synthesis of porous Pt/NiO nanocubes, certain amount of $Pt(NO_3)_2.xH_2O$ and 0.057 mol of $Ni(NO_3)_2{\cdot}6H_2O$ were dissolved in ~ 8 g of water. 10 g of porous silica template was dispersed in the mixed green solution. Afterward, the solution was dried at 100 °C for 4 h and the obtained green silica powder transformed into black after calcination at 500 °C for 2 h. Silica template was leached by NaOH etching, and porous Pt/NiO nanocubes were obtained after washing and drying. Two electrocatalysts with different theoretical Pt loading amount were prepared and denoted as 0.5 wt.% Pt/NiO, and 1 wt.% Pt/NiO, respectively. Pure porous NiO and PtO_2 were also prepared in a similar way. A single batch of 200 g 0.5 wt.% Pt/NiO was prepared by simply increasing the amount of chemicals. For synthesis of ALD-Pt/NiO, the porous NiO (1.5 g) were well dispersed in 100 ml ethanol by ultrasonication, and then 4 mL of the suspension was dropped onto a quartz wafer (10 cm × 10 cm). After drying at ambient temperature, the quartz wafer was then transferred to a home-made ALD chamber for Pt deposition. Ultrahigh purity nitrogen was used as the carrier and purge gas. Pt ALD was performed by sequential exposure of the sample to $MeCpPtMe_3$ (Strem Chemicals, 99%) and ozone produced using an ozone generator, with a pulse time of 0.5 s, an exposure time of 10 s, and a nitrogen purge time of 25 s for $MeCpPtMe_3$ and a pulse time of 1 s, an exposure time of 10 s, and a nitrogen purge time of 25 s for O_3. The deposition temperature for Pt was maintained at 240 °C and that for $MeCpPtMe_3$ was maintained at 60 °C to provide enough vapor pressure.

Characterization. The phases of Pt/NiO nanocubes were identified by powder wide angle XRD using Rigaku Ultima IV diffractometer with Cu Kα radiation (λ= 0.154178 nm). The surface and crystal structures of doped or un-doped NiO nanocubes were characterized by SEM (Zeiss Supra 55VP), and TEM (FEI Tecnai G2). HAADF STEM images were obtained on a JEOL JEM-ARM200F STEM/TEM, equipped with a CEOS probe corrector and with a guaranteed resolution of 0.08 nm. Prior to the examination, the samples were dry dispersed on the copper grid coated with a thin holey carbon film. X-ray photoelectron spectroscopy (XPS) measurements were performed on a Thermo/K-Alpha XPS using monochromatic Al Kα X-ray source. All binding energies were calibrated by setting C 1s at 284.8 eV. Nitrogen sorption isotherms of samples were obtained with a Micromeritics system. The multipoint Braunauer-Emmett-Teller (BET) method was applied to determine the specific surface areas of all the samples. The decomposition behavior of metal nitrates in dried SiO_2 supported samples were examined by the TGA on a TG analyzer in dry air in the range of 30-800 °C with a heating rate of 10 °C /min. An inductively coupled plasma optical emission spectrometer (ICP-OES, Perkin Elmer Optima 8000) was applied to analyze the element composition of electrocatalysts and used electrolyte.

The local atomic and electronic structures around Pt atoms in the samples of 0.5 wt.% Pt/NiO and 1 wt.% Pt/NiO were investigated by X-ray absorption fine structure (XAFS) at the Pt L3-edge and Ni K-edge. XAFS measurements were performed on Beam line BL14W1 at the Shanghai Synchrotron Radiation Facility (SSRF) with the electron storage ring operated at 3.5Gev, equipped with a double Si (111) crystal monochromator. High-order harmonics were successfully inhibited using a harmonic suppression mirror. Pt foil and PtO_2 were used as reference samples and measured in the transmission mode. Samples for Ni K-edge were measured by transmission mode, while Pt L3-edge for all Pt containing samples were collected by fluorescence mode. Before measurement, appropriate amounts of samples were finely crushed and pressed to form a disk. The disk was then sealed with Kapton membrane. A cell was employed for collecting XAFS data at RT in flow of He operating at 1 bar. All the XAFS data analysis was carried out using the Ifeffit software package to calibrate the energy, to correct the background signal and to normalize the intensity. The normalized EXAFS function, $\chi(E)$, was transformed from energy space to K-space, $\chi(k)$, where k is the photoelectron wave vector. The $\chi(k)$ data were multiplied by k^3 to compensate for damping of EXAFS oscillations in the high k-region. The backscattering amplitude and phase shift were obtained from theoretical calculation using the FEFF code. S02 value of 0.81 and 0.82 were obtained from fitting to Pt standard samples and Ni standard samples. From the analysis, structural parameters, such as the coordination numbers (N), bond distance (R), Debye-Waller factor and inner potential shift could be calculated.

Electrochemical measurements. All electrochemical tests were performed on a Princeton Verstat 4000 electrochemical work station. In order to avoid the effect of trace iron, the polytetrafluoroethylene electrochemical cell and beakers were cleaned by 0.5 M H_2SO_4 and rinsed with deionized water (18.2 MΩ) for at least 3 times. The 1 M KOH electrolyte was prepared by dissolving KOH (semiconductor grade 99.99% trace metal basis, Sigma Aldrich) in the deionized water (18.2 MΩ) as well as the usage of an Fe-absorbent (i.e. $Ni(OH)_2$) by following previously reported method.[S1, S2] 5 mg of sample powder were dispersed in 1 ml of 3:1 v/v water/isopropanol solution. Subsequently, 16 µl of 5 wt.% Nafion solution was added. The mixed solution was sonicated for 30 min for obtain a homogeneous ink. The working electrode was prepared by uniformly drop casting 20 µl of the catalyst ink onto the carbon paper and then baked at 60 °C for 30 min. Cyclic voltammetry (CV), and electrochemical impedance spectroscopy (EIS) measurements were carried out using a typical 3-electrode configuration with a Pt plate as the counter electrode and an Ag/AgCl electrode as the reference electrode. The CV curves were recorded at a sweep rate of 10 or 100 mV s^{-1} and give number of cycles between 0.01 and 2.01 V vs. RHE at 25 °C. The overpotential at 10 mA cm^{-2} or 120 mA cm^{-2} and Tafel plots were obtained by using the cathode sweep of CV curves to avoid the interference of oxidation peaks. The EIS measurements were performed by applying an AC voltage in the frequency ranges from 100 kHz to 0.1Hz. The potentials reported in our study were referenced to the reversible hydrogen electrode (RHE) through RHE calibration, E(RHE) = E(Ag/AgCl) + 1.01V. The electrolyte resistance value used for the ohmic drop compensation is in the range of 2.0-2.5 Ω.

Details for Stochastic Surface Walking (SSW)

In this work, the spinel-to-layer solid phase transition was investigated using the SSW reaction pathway sampling method.[S3-9] The SSW algorithm has an automated climbing mechanism to manipulate a structure configuration from a minimum to a high-energy configuration along one random mode direction, inherits the idea of bias-potential driven constrained-Broyden-dimer (BP-CBD) method for TS location.[S10] In one particular SSW step, labeled as i, a modified PES $V_{m\text{-}to\text{-}n}$ (n is the index of the bias potential, n=1,2⋯H), as shown in the following equation, is utilized for moving from the current minimum, R_i^m to a high energy configuration R_i^H (the climbing), in which a series of bias Gaussian potential v_n is added one by one consecutively along the direction N_i^n.

$$V_{m-to-H} = V_{real} + \sum_{n=1}^{H} v_n = V_{real} + \sum_{n=1}^{H} w_n \times \exp\left[-\left((\mathbf{R}^t - \mathbf{R}_t^{n-1})\cdot \mathbf{N}_i^n\right)^2 \Big/ \left(2 \times ds^2\right)\right]$$

where R is the coordination vector of the structure and V_{real} represents the unmodified PES; R_t^n are the n^{th} local minima along the movement trajectory on the modified PES that is created after adding n Gaussian functions. The Gaussian function is controlled by its height w and its width ds, and is always added along one particular walking direction as defined by N^n. Once the R_i^H is reached, all bias potentials are removed and the local optimization is performed to quench the structure to a new minimum. This algorithm was described in our previous work in detail.[S8-S10]

The procedure to determine the phase transition pathway includes two steps: (i) SSW sampling to collect all possible pairs of initial states and final states (IS/FS pair); (ii) variable-cell double-ended surface walking (VC-DESW) method to locate the transition state (TS) in low energy reaction pathway. The SSW was utilized recently in finding the lowest energy pathway of solid phase transition, such as ZrO_2, [S5] TiO_2,[S4] and MnO_2[S3]. In previous study, [S11] we have identified the pathway of the same phase transition occurs on $H_{0.5}MnO_2$ (spinel $H_{0.5}MnO_2$ → layered δ-MnO_2). Due to the similarity of both processes, we did not perform SSW sampling anymore to generate IS/FS pair. Alternatively, we adopted the IS / FS pair from $H_{0.5}MnO_2$, replacing Mn by Ni cations, and then determine the TS using VC-DESW. All located TSs were further confirmed by extrapolating the TS towards the IS and FS and also the numerical vibrational frequency analysis.

Details for DFT Calculations

All DFT calculations were carried out within the periodic plane wave framework as implemented in Vienna ab initio simulation package (VASP). The electron-ion interaction was represented by the projector augmented wave (PAW) and the kinetic energy cutoff of plane wave was set as 500 eV. The geometry optimization and the energetic profiles for OER were based on the exchange-correlation functional GGA-PBE with on-site Coulomb repulsion (PBE+U). The effective U-J terms (U_{eff}) as determined by linear response theory was set as 5.5 eV for Ni. The geometry convergence criterion was set as 0.01 eV/Å for the maximal component of force. For all $H_{0.5}NiO_2$ systems, spin-polarization has been considered to identify the ground state electronic configuration. The initial magnetic ordering of the γ-NiOOH is set to be ferromagnetic, while it is antiferromagnetic for NiO. The k-point mesh utilized was up to (4 × 4 × 4) in the Monkhorst−Pack scheme, which was verified to be accurate enough for these bulk systems.

Calculation Details for Theoretical Overpotential

To calculate the OER overpotential, we use the Standard Hydrogen Electrode (SHE: $H^+ + e^- \rightarrow {}^{1}/_{2}H_2$, pH = 0, p = 1 bar, T = 298.15K) as reference, where we get

$$\Delta G^{o}_{SHE} = {}^{1}/_{2}G^{o}[H_2] - G^{o}[H^+] - G^{o}[e^-] = 0 \tag{1}$$

$$G^{o}[H^+] = {}^{1}/_{2}G^{o}[H_2] - G^{o}[e^-] = {}^{1}/_{2}G^{o}[H_2] + \Phi_w \tag{2}$$

where $G^{o}[H_2]$, $G^{o}[H^+]$ are the Gibbs free energy change of H_2 and H^+ in standard condition. Φ_w refers to the work function of charged Pt in SHE (i.e. the absolute electrode potential of SHE vs. vacuum level), which is a constant of 4.44eV recommended by IUPAC. while Φ_w is the work function of Pt electrode in SHE. For other pH, the free energy $G[H^+]$ can be calculated as

$$G[H^+] = G^{o}[H^+] - 0.059pH \tag{3}$$

Using Eq. 2-3, we can derive the ΔG of an electrochemical half-reaction as described by formula 4.

$$H_nA \rightarrow A + nH^+ + ne^- \tag{4}$$

The ΔG is written as

$$\Delta G = G[A] + nG[H^+] + nG[e^-] - G[H_nA] \tag{5}$$

Substituting Eq. 2 into Eq. 5, we get

$$\Delta G = G[A] + n({}^{1}/_{2}G^{o}[H_2] - G[e^-]_{SHE} - 0.059pH) + nG[e^-] - G[H_nA]$$

$$= G[A] + {}^{n}/_{2}G^{o}[H_2] - n\times0.059pH + n(G[e^-] + \Phi_w) - G[H_nA]$$

$$= G[\mathrm{A}] + {}^{n}/{}_{2}G^{o}[\mathrm{H_2}] - G[\mathrm{H_nA}] - \mathrm{n}|\mathrm{e}|\mathrm{U} - {}^{n}/{}_{2}\times 0.059\mathrm{pH} \quad (6)$$

Setting $\Delta G = 0$, the parameter U then is the electrochemical potential for half-reaction of $H_nA \rightarrow A + nH^+ + ne^-$. The rate-determining step is then the elementary step with most positive ΔG, and the corresponding theoretical overpotential (η) is calculated by Eq. 7.

$$\eta = \mathrm{U} - 1.23 \quad (7)$$

where 1.23 is the electrochemical potential for OER in standard condition.

Calculation Details for Phase Diagram of NiO, Ni_3O_4, $H_{0.5}NiO_2$ and NiO_2

The phase diagram of NiO, Ni_3O_4, $H_{0.5}NiO_2$ and NiO_2 involves three consecutive reactions from rocksalt NiO to spinel Ni_3O_4, $H_{0.5}NiO_2$ and NiO_2 following the chemical formula below.

$$4\mathrm{NiO} \rightarrow \mathrm{Ni_3O_4} + \mathrm{Ni^{2+}} + 2\mathrm{e^-} \quad (8)$$

$$2\mathrm{Ni_3O_4} + 2\mathrm{H^+} \rightarrow 4\mathrm{H_{0.5}NiO_2} + 2\mathrm{Ni^{2+}} + 2\mathrm{e^-} \quad (9)$$

$$2\mathrm{H_{0.5}NiO_2} \rightarrow 2\mathrm{NiO_2} + \mathrm{H^+} + \mathrm{e^-} \quad (10)$$

Using NiO phase as reference, we can further write the Eq. 9-10 as

$$4\mathrm{NiO} + \mathrm{H^+} \rightarrow 2\mathrm{H_{0.5}NiO_2} + 2\mathrm{Ni^{2+}} + 3\mathrm{e^-} \quad (11)$$

$$4\mathrm{NiO} \rightarrow 2\mathrm{NiO_2} + 2\mathrm{Ni^{2+}} + 4\mathrm{e^-} \quad (12)$$

The free energy change in reactions of 8, 11, 12 can then be calculated by following formula.

$$\Delta G[\mathrm{Ni_3O_4}] = G[\mathrm{Ni_3O_4}] + G[\mathrm{Ni^{2+}}] + 2G[\mathrm{e^-}] - 4G[\mathrm{NiO}] \quad (13)$$

$$\Delta G[\mathrm{H_{0.25}NiO_2}] = 2G[\mathrm{H_{0.25}NiO_2}] + 2G[\mathrm{Ni^{2+}}] + 3G[\mathrm{e^-}] - G[\mathrm{H^+}] - 4G[\mathrm{NiO}] \quad (14)$$

$$\Delta G[\mathrm{NiO_2}] = 2G[\mathrm{NiO_2}] + G[\mathrm{Ni^{2+}}] + 4G[\mathrm{e^-}] - 4G[\mathrm{NiO}] \quad (15)$$

$G[H^+]$ can be calculated by CHE as shown in previous section. While for $G[Ni^{2+}]$, we use the electrochemical equilibrium of ($Ni \rightarrow Ni^{2+} + 2e^-$) at the potential of $E^{o}_{Ni^{2+}/Ni}$.

$$0 = G^{o}[\mathrm{Ni^{2+}}] + 2G^{o}[\mathrm{e^-}] - G^{o}[\mathrm{Ni}] \quad = G^{o}[\mathrm{Ni^{2+}}] - 2(|\mathrm{e}|E^{o}_{\mathrm{Ni^{2+}/Ni}} + \Phi_{\mathrm{w}}) - G^{o}[\mathrm{Ni}] \quad (16)$$

So we get

$$G[\mathrm{Ni^{2+}}] = G^{o}[\mathrm{Ni}] + 2(|\mathrm{e}|E^{o}_{\mathrm{Ni^{2+}/Ni}} + \Phi_{\mathrm{w}}) \quad (17)$$

The relative stabilities of $H_{0.5}NiO_2$ and NiO_2 compared with NiO can then be estimated by following formula.

$$\Delta G[\mathrm{Ni_3O_4}] = G[\mathrm{Ni_3O_4}] + G^{o}[\mathrm{Ni}] + 2|\mathrm{e}|E^{o}_{\mathrm{Ni^{2+}/Ni}} - 2|\mathrm{e}|\mathrm{U} - 4G[\mathrm{NiO}] \quad (18)$$

$$\Delta G[\mathrm{H_{0.25}NiO_2}] = 2G[\mathrm{H_{0.25}NiO_2}] + 2G^{o}[\mathrm{Ni}] + 2|\mathrm{e}|E^{o}_{\mathrm{Ni^{2+}/Ni}} - 3|\mathrm{e}|\mathrm{U} - {}^{n}/{}_{2}G[\mathrm{H_2}] - 4G[\mathrm{NiO}] \quad (19)$$

$$\Delta G[\mathrm{NiO_2}] = 2G[\mathrm{NiO_2}] + G^{o}[\mathrm{Ni}] + 2|\mathrm{e}|E^{o}_{\mathrm{Ni^{2+}/Ni}} - 4|\mathrm{e}|\mathrm{U} - 4G[\mathrm{NiO}] \quad (20)$$

By plotting ΔG vs. U, we finally get the phase diagram of NiO, Ni_3O_4, $H_{0.5}MnO_2$ and NiO_2. It should be mentioned that the line for NiO is horizontal, since NiO is the reference state where the free energy change is zero for this component.

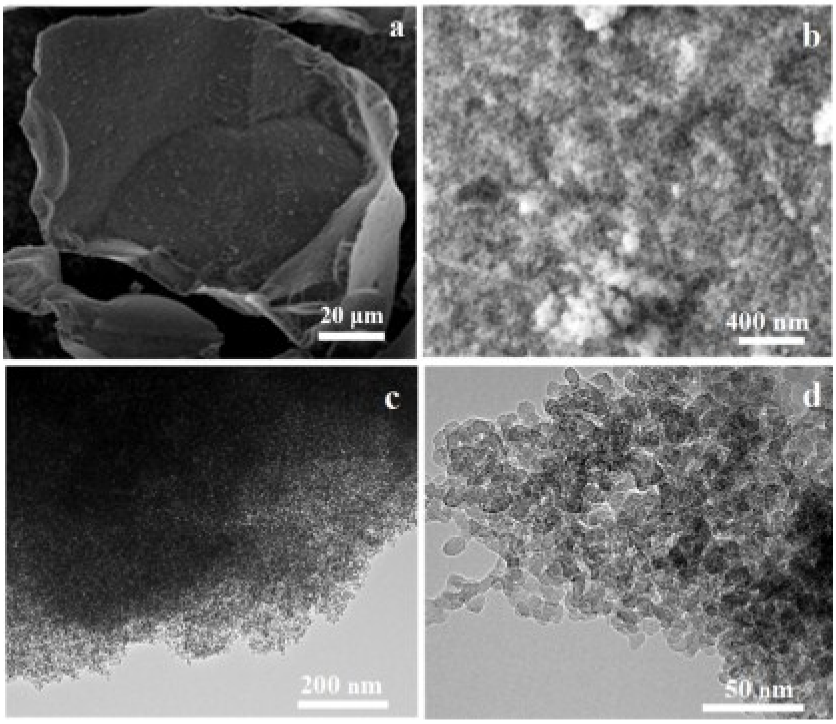

Figure S1. (a, b) SEM and (c, d) TEM images of commercial silica template at different magnifications.

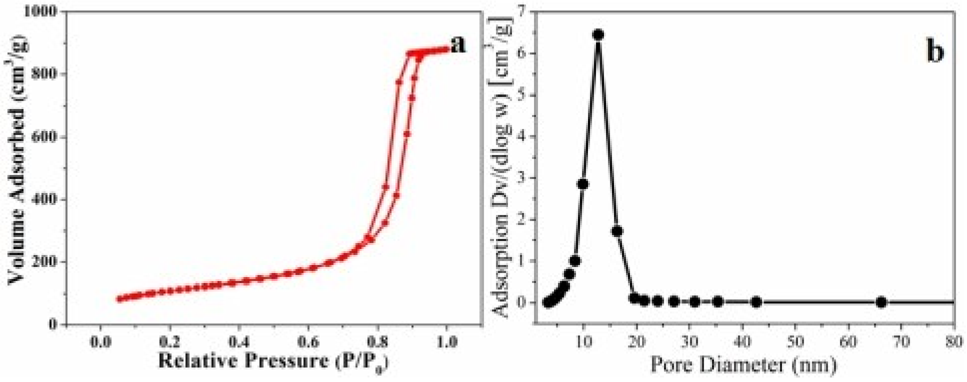

Figure S2. (a) N_2 adsorption-desorption isotherms and (b) pore size distribution of commercial silica template.

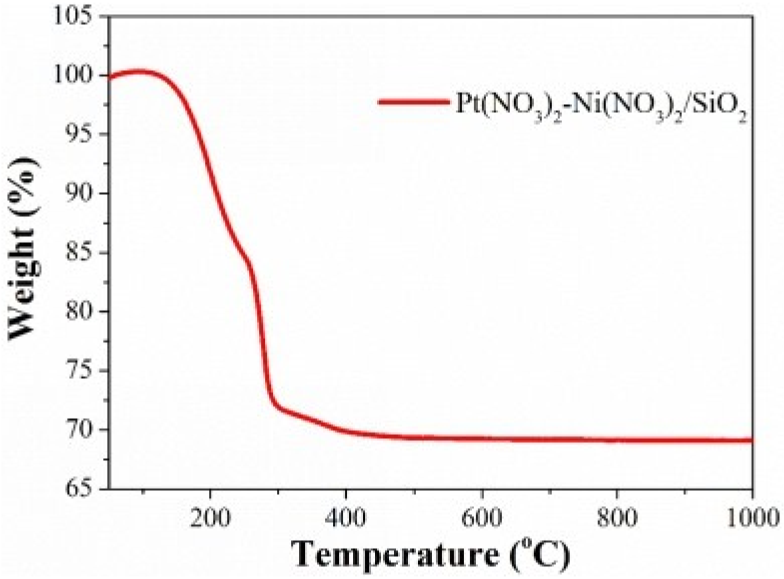

Figure S3. Thermogravimetric analysis (TGA) curve of porous silica impregnated with $Ni(NO_3)_2$ and $Pt(NO_3)_2$ after drying.

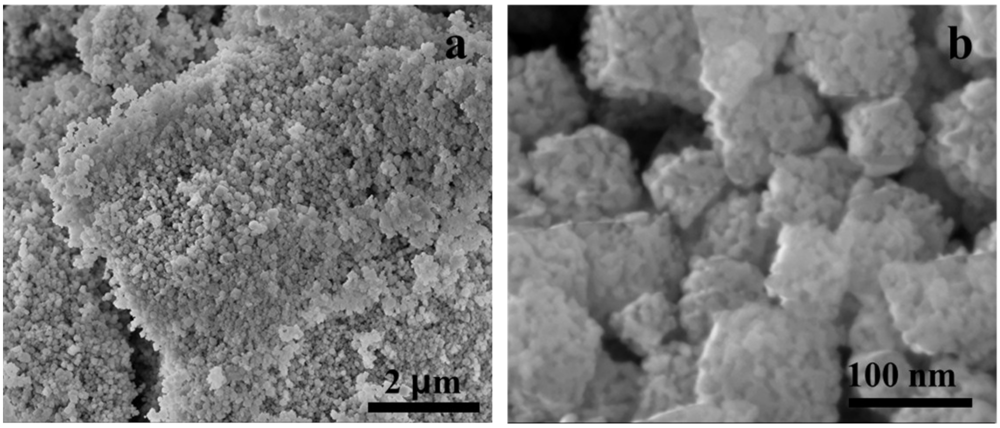

Figure S4. SEM images of pure NiO at different magnifications.

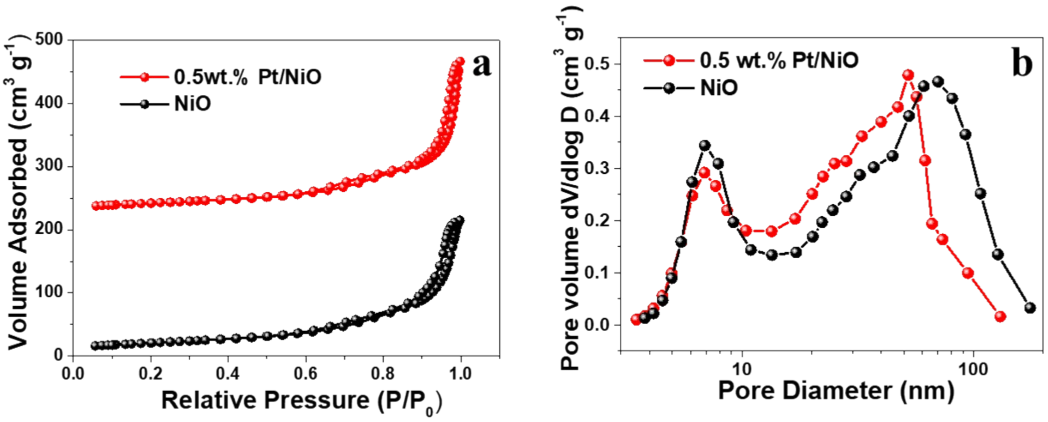

Figure S5. (a) Nitrogen adsorption and desorption isotherms and (b) the corresponding pore size distribution of pure NiO and 0.5 wt.% Pt/NiO nanocubes.

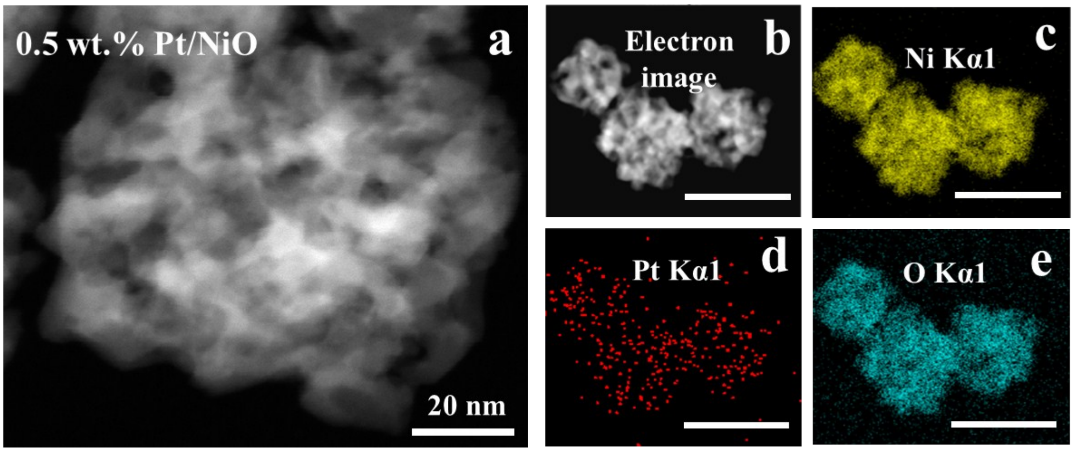

Figure S6. STEM image and relative EDS mappings of 0.5 wt.% Pt/NiO. The EDS signals of Ni, Pt and O elements are displayed in yellow, red and blue, respectively. Scale bars in (b) – (e) is 50 nm.

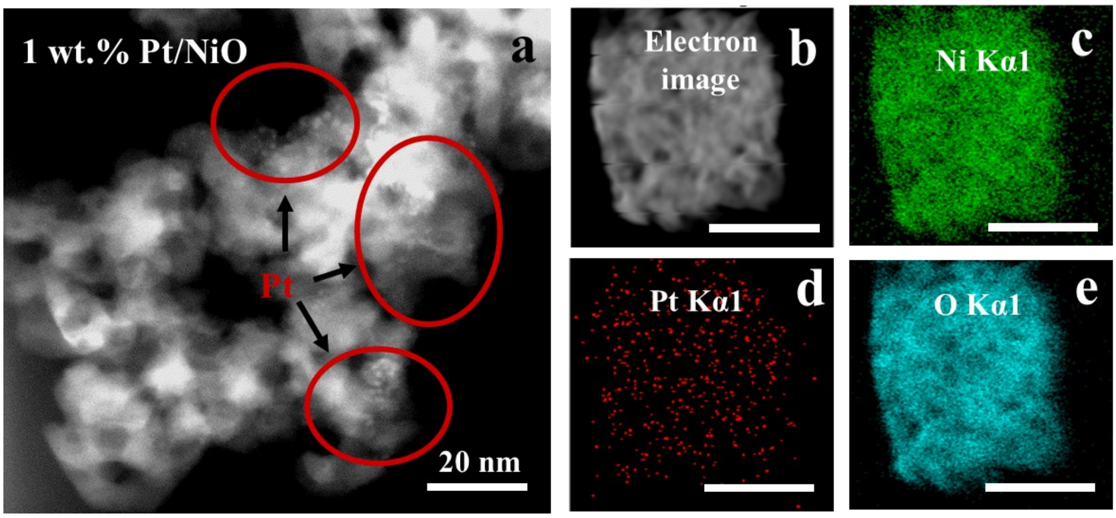

Figure S7. STEM image and relative EDS mappings of 1 wt.% Pt/NiO. The EDS signals of Ni, Pt and O elements are displayed in green, red and blue, respectively. Scale bars in (b) – (e) is 50 nm.

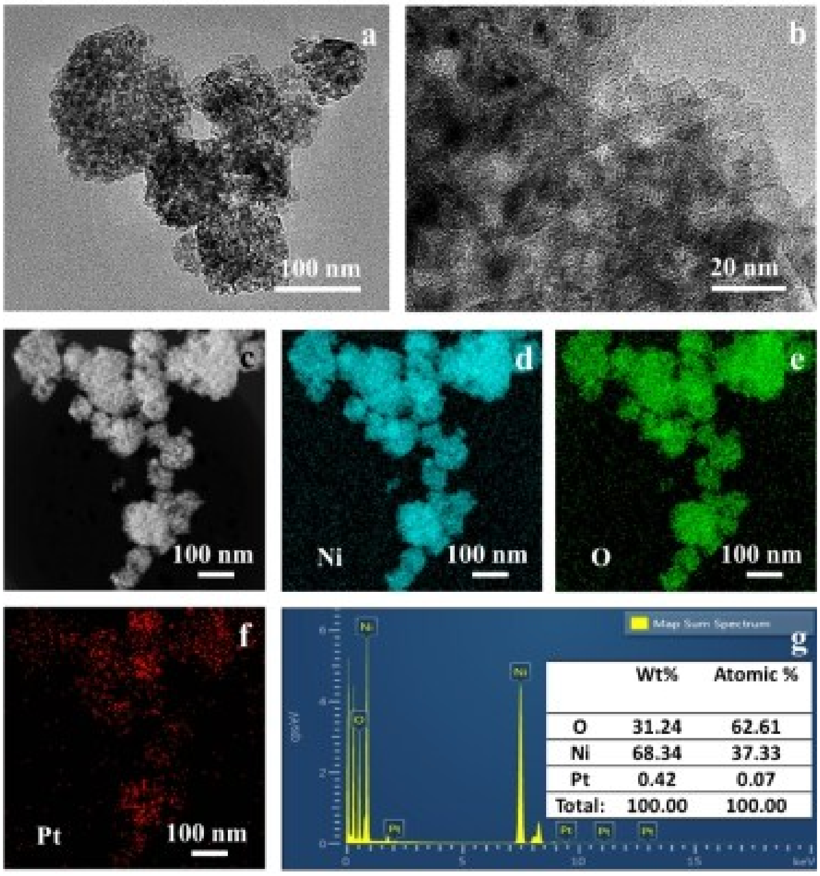

	Wt%	Atomic %
O	31.24	62.61
Ni	68.34	37.33
Pt	0.42	0.07
Total:	100.00	100.00

Figure S8. TEM (a, b), STEM (c) images, (d-f) element mappings and (g) EDS data of ALD-Pt/NiO.

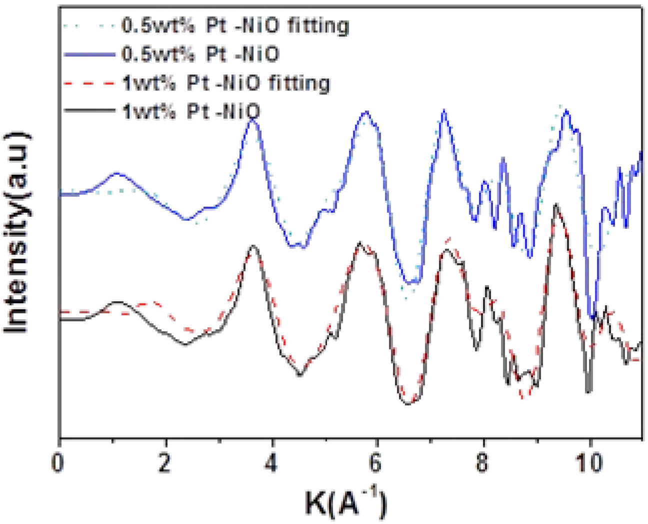

Figure S9. The original and fitting EXAFS signal χ(κ), weighted with k^3 for two samples. The solid lines are experimental data. The dashed lines are fitting data.

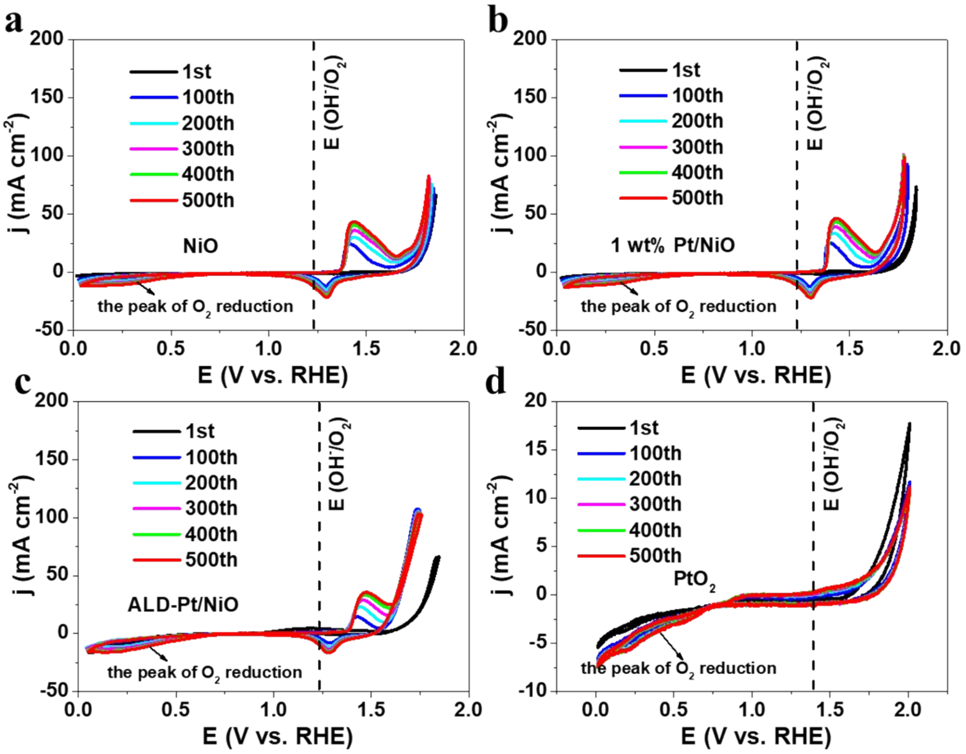

Figure S10. CV curves of (a) NiO, (b) 1 wt.% Pt/NiO, (c) ALD-Pt/NiO, and (d) porous PtO_2 recorded at the 1st, 100th, 200th, 300th, 400th and 500th cycle. The CV data was recorded at a sweep rate of 100 mV s^{-1}. The catalyst loading was set as 0.1 mg cm^{-2}.

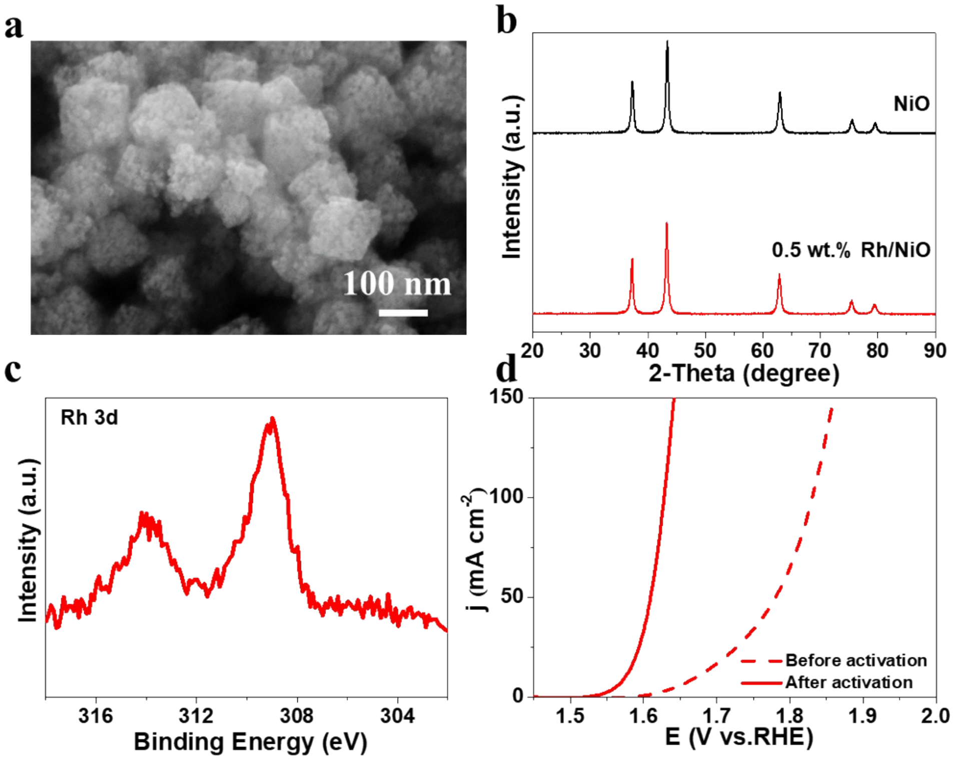

Figure S11. (a) SEM image, (b) XRD pattern and (c) Rh 3d XPS spectra of 0.5 wt.% Rh/NiO. (d) LSV curves of Rh/NiO before and after 500 cycles.

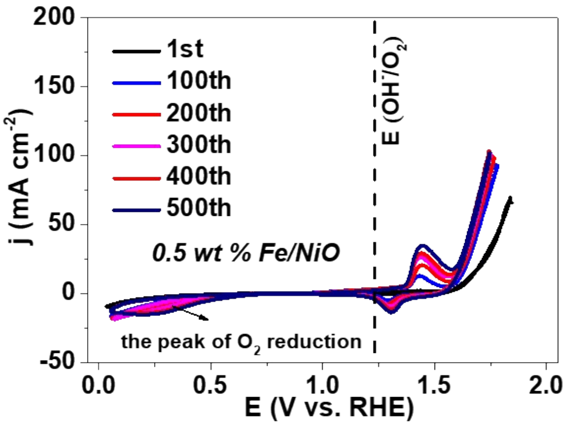

Figure. S12. CV curves of 0.5 wt.% Fe/NiO recorded at the 1st, 100th, 200th, 300th, 400th and 500th cycle. The CV data was recorded at a sweep rate of 100 mV s^{-1}. The catalyst loading was set as 0.1 mg cm^{-2}.

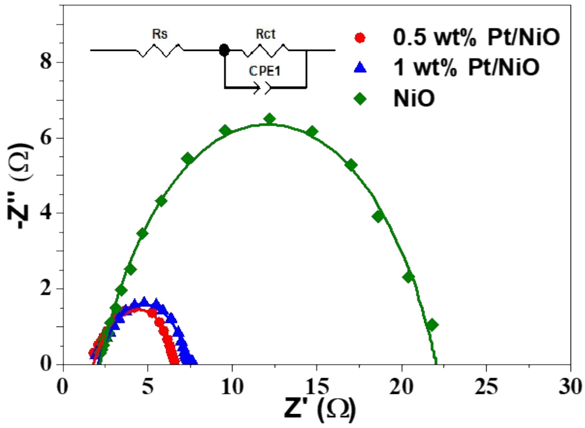

Figure. S13. EIS Nyquist plots of NiO, 0.5wt. % Pt/NiO, and 1 wt. % Pt/NiO electrode before 500 cycles.

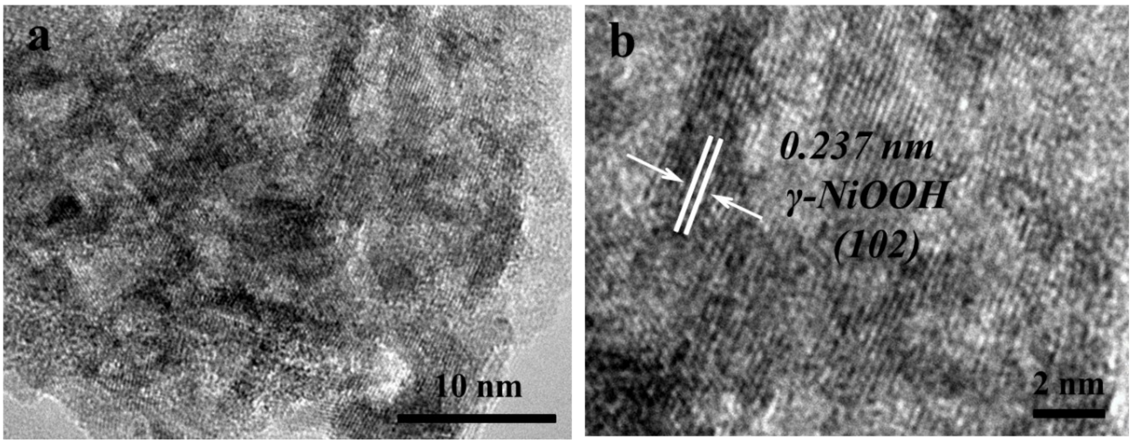

Figure. S14. (a) TEM images of 0.5 wt.% Pt/NiO catalysts after 500 electrochemical cycles. (b) is the magnified view of (a).

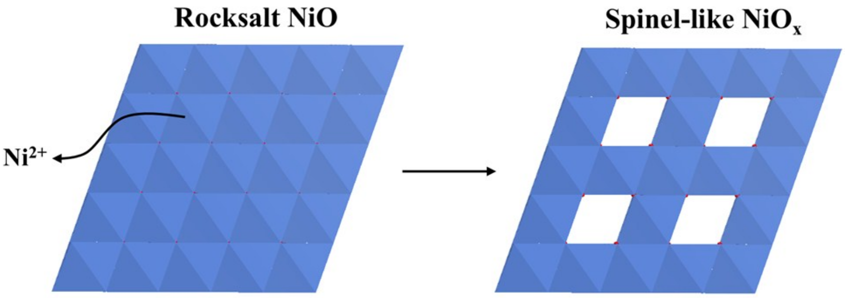

Figure S15. Structural evolution from rocksalt to spinel-like structures.

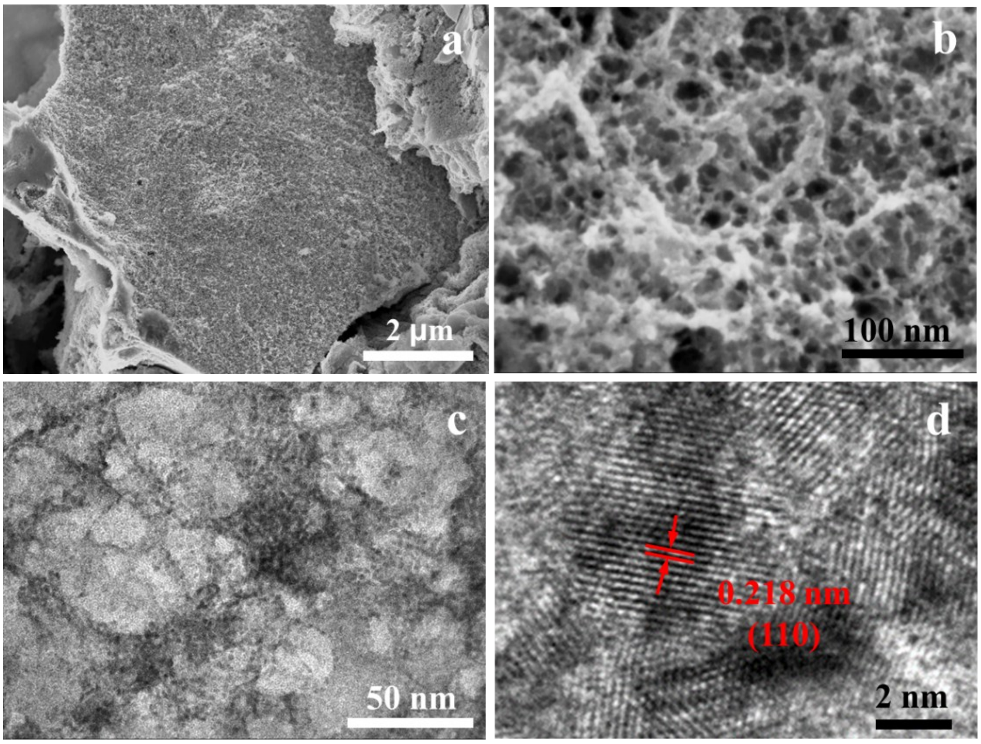

Figure S16. TEM images of platinum oxide at different magnifications.

Table S1. Structure parameters from the EXAFS spectra analysis at the Pt L3-edge for 0.5 wt.% Pt/NiO and 1 wt.% Pt/NiO, and the reference of Pt foil and PtO_2.

Sample	Shell	N	R(Å)	$\Delta\sigma^2$(Å^2)	ΔE_0(eV)	R-factor
Pt foil	Pt-Pt	12	2.78			
PtO_2	Pt-O	6	2.07			
	Pt-Pt	6	3.10			
	Pt-O_2	6	3.59			
NiO	Ni-O	6	2.09			
	Ni-Ni	12	2.96			
0.5 wt.%	Pt-O	6.0	2.00	0.003	11.0	0.0018
Pt/NiO	Pt-Ni	5.5	3.00	0.006	3.5	
1 wt.%	Pt-O	6.0	2.01	0.002	10.0	0.0019
Pt/NiO	Pt-Ni	2.0	3.00	0.005	1.4	
	Pt-Pt	4.0	3.09	0.003	10.0	

N, coordination number; R, distance between absorber and back scatter atoms; $\Delta\sigma^2$, change in the Debye-Waller factor value relative to the Debye-Waller factor of the reference compound; ΔE_0, inner potential correction to account for the difference in the inner potential between the sample and reference compound. Error bounds (accuracies) that characterize the structural parameters obtained by EXAFS spectroscopy were estimated as N, ±20%; R, ±1%; $\Delta\sigma^2$, ±20%; ΔE_0, ±20%. Pt foil parameters from data_77654-ICSD; r space fit, Δk =2.417-10.813Å-1, Δr =1.0-3.2, 12 statistically justified parameters; S02 fitting from Pt foil defined as 0.81.

Table S2. EXAFS parameters of different candidate models of two samples.

sample	Shell	N	R(Å)	$\Delta\sigma^2$(Å^2)	ΔE_0(eV)	R-factor
Pt foil	Pt-Pt	12	2.78			
PtO$_2$	Pt-O	6	2.07			
	Pt-Pt	6	3.10			
	Pt-O$_2$	6	3.59			
NiO	Ni-O	6	2.09			
	Ni-Ni	12	2.96			
0.5 wt.% Pt/NiO (Model I)	Pt-O	6.0	2.00	0.003	11.0	0.0018
	Pt-Ni	5.5	3.00	0.006	3.5	
0.5 wt.% Pt/NiO (Model II)	Pt-O	6.0	2.00	0.003	11.0	0.062
	Pt-Pt	6.0	3.09	0.008	10.0	
0.5 wt.% Pt/NiO (Model III)	Pt-O	6.0	2.00	0.003	10.5	0.036
	Pt-Ni	3.0	2.97	0.003	9.6	
	Pt-Pt	3.0	3.10	0.008	1.0	
1 wt.% Pt/NiO (Model I)	Pt-O	6.0	2.00	0.003	11.0	0.056
	Pt-Ni	5.5	3.00	0.006	3.5	
1 wt.% Pt/NiO (Model II)	Pt-O	6.0	2.01	0.002	10.0	0.039
	Pt-Pt	6.0	3.10	0.003	13.0	
1 wt.% Pt/NiO (Model III)	Pt-O	6.0	2.01	0.002	10.0	0.0019
	Pt-Ni	2.0	3.00	0.005	1.4	
	Pt-Pt	4.0	3.09	0.003	10.0	

Supporting Reference

S1. L. J. Enman, M. S. Burke, A. S. Batchellor and S. W. Boettcher, *ACS Catal.*, 2016, **6**, 2416-2423.

S2. L. Trotochaud, S. L. Young, J. K. Ranney and S. W. Boettcher, *J. Am. Chem. Soc.*, 2014, **136**, 6744-6753.

S3. Y.-F. Li, S.-C. Zhu and Z.-P. Liu, *J. Am. Chem. Soc.,* 2016, **138**, 5371-5379.

S4. S.-C. Zhu, S.-H. Xie and Z.-P. Liu, *J. Am. Chem. Soc.*, 2015, **137**, 11532-11539.

S5. S.-H. Guan, X.-J. Zhang and Z.-P. Liu, *J. Am. Chem. Soc.,* 2015, **137**, 8010-8013.

S6. X.-J. Zhang and Z.-P. Liu, *J. Chem. Theo. Comput.*, 2015, **11**, 4885-4894.

S7. X.-J. Zhang, C. Shang and Z.-P. Liu, *J. Chem. Theo. Comput.*, 2013, **9**, 5745-5753.

S8. C. Shang, X.-J. Zhang and Z.-P. Liu, *Phys. Chem. Chem. Phys.*, 2014,**16**, 17845-17856.

S9. C. Shang and Z.-P. Liu, *J. Chem. Theo. Comput.*, 2013, **9**, 1838-1845.

S10. C. Shang and Z.-P. Liu, *J. Chem. Theo. Comput.*, 2012, **8**, 2215-2222.

S11. Y.-F. Li, Z.-P. Liu, *J. Am. Chem. Soc.*, 2018, **140**, 1783-1792.